applied optics

A path to high-quality imaging through disordered optical fibers: a review

Jian Zhao,[1,*] Mostafa Peysokhan,[2,3] Jose Enrique Antonio-Lopez,[1] Yangyang Sun,[1] Behnam Abaie,[2,3,4] Arash Mafi,[2,3] Rodrigo Amezcua Correa,[1] Shuo Pang,[1] and Axel Schülzgen[1]

[1]CREOL, College of Optics and Photonics, University of Central Florida, Orlando, Florida 32816, USA
[2]Department of Physics & Astronomy, University of New Mexico, Albuquerque, New Mexico 87131, USA
[3]Center for High Technology Materials (CHTM), University of New Mexico, Albuquerque, New Mexico 87106, USA
[4]CNC Program, Stanford University, Stanford, California 94305, USA
*Corresponding author: jianzhao@knights.ucf.edu

Received 3 December 2018; revised 4 March 2019; accepted 7 March 2019; posted 7 March 2019 (Doc. ID 353360); published 9 April 2019

In this paper, we review recent progress in disordered optical fiber featuring transverse Anderson localization and its applications for imaging. Anderson localizing optical fiber has a transversely random but longitudinally uniform refractive index profile. The strong scattering from the transversely disordered refractive index profiles generates thousands of guiding modes that are spatially isolated and mainly demonstrate single-mode properties. By making use of these beam transmission channels, robust and high-fidelity imaging transport can be realized. The first disordered optical fiber of this type, the polymer Anderson localizing optical fiber, has been utilized to demonstrate better imaging performance than some of the commercial multicore fibers within a few centimeters transmission distance. To obtain longer transmission lengths and better imaging qualities, glass–air disordered optical fibers are desirable due to their lower loss and larger refractive index contrast. Recently developed high air-filling fraction glass–air disordered fiber can provide bending-independent and high-quality image transport through a meter-long transmission distance. By integrating a deep-learning algorithm with glass–air disordered fiber, a fully flexible, artifact-free, and lensless fiber imaging system is demonstrated, with potential benefits for biomedical and clinical applications. Future research will focus on optimizing structural parameters of disordered optical fiber as well as developing more efficient deep-learning algorithms to further improve the imaging performance.

https://doi.org/10.1364/AO.58.000D50

1. INTRODUCTION

Anderson localization describes the absence of diffusive wave transport in a highly disordered medium and was first introduced by Anderson in the context of electron motion [1]. In Anderson's picture, the interference of electron waves experiencing multiple scattering by random defects in the potential landscape results in electronic states localized in space. Since Anderson localization is a consequence of the wave nature of electrons, this concept can also be applied to classical wave systems, including acoustics, elastics, electromagnetics, and optics [2–5]. Among all classical wave systems, the localization of light has attracted a lot of attention, and related progress has demonstrated its great potential in device-level applications [6–15]. However, it is difficult to observe the localization of light in three-dimensional systems due to limitations set by the Ioffe–Regel criterion [16]. This criterion states the following: in order for localization to occur, the scattering must be strong enough so that $kl^* \sim 1$, where k is the effective wavevector in the medium and l^* is the mean free path. But this condition is considerably relaxed in two-dimensional (2D) systems [17,18]. Optical waves can be localized in 2D disordered systems, and the localization length ξ, which is the effective beam width in the transverse plane, is given by $\xi = l^* \exp(\pi k\perp l^*/2)$, where the mean free path l^* relates to the refractive index fluctuations and $k\perp$ is the transverse component of the wavevector k. In a quasi-2D system where the randomness is only limited to the transverse plane, the transverse wavevector component $k\perp$ can be 10–100 times smaller than k. Therefore, even if the mean free path is much larger than the wavelength, localization can still occur [18,19].

Transverse Anderson localization (TAL) was first proposed numerically by Abdullaev and Abdullaev and De Raedt *et al.* [17,20]. In particular, the refractive index in the disordered system introduced by De Raedt *et al.* is distributed randomly in the transverse plane and invariantly along the longitudinal direction. The optical beam propagating along the longitudinal direction of such a system can maintain a finite beam cross section due to the TAL in the transverse plane, which resembles

the beam propagation in waveguide devices. It has also been found that the localization length depends on the refractive index contrast and the materials' filling fraction [17]. The first experimental observation of TAL of light in a similar system was demonstrated by Segev's team in 2007 [18]. In this pioneering work, they use a probe beam to investigate TAL in a photorefractive crystal. The refractive index profile of this crystal is randomly distributed in the transverse plane and invariant longitudinally. However, the small photoinduced refractive index variations ($\sim 10^{-4}$) result in rather large localization beam radii with a large standard deviation among different realizations of the random refractive index profile. Although the TAL beam radius is meaningful in a statistical averaging sense, the self-averaging behavior can guarantee similar levels of localization for different realizations of random profiles if large refractive index variations are introduced to produce strong wave localization [19,21–24]. In this case, one realization of the statistically identical ensemble of TAL waveguides is practically equivalent to the ensemble average. Therefore, large refractive index variations are desired for pushing TAL optical waveguides to real applications.

The first TAL disordered waveguide with large refractive index fluctuations (~0.1) was developed by Mafi's team in 2012 [19]. This TAL device is a disordered polymer Anderson localizing optical fiber (pALOF) fabricated by randomly mixing 40,000 pieces of polymethyl methacrylate fibers and 40,000 pieces of polystyrene fibers. The localized beam radius of pALOF is sufficiently small and comparable to a typical index-guiding optical fiber. Moreover, the large index contrast inside pALOF reduces the sample-to-sample variations of localized beam radii to a level that can satisfy image transmission requirements. Besides large refractive index fluctuations, Karbasi *et al.* further found through a numerical study that an ~50% materials filling fraction is desirable for generating small localized beam radii [21,23]. Based on a one-dimensional waveguide model, it is also numerically confirmed that the optimal feature size might be around twice the wavelength of operation, and the quality of image transport can be improved in disordered waveguides compared to periodic waveguide structures [23,25]. Recent research on the mode properties of disordered optical fiber further unveils that most of the guided modes in pALOF exhibit single-mode properties [26]. In particular, Abaie *et al.* reveal that highly localized modes in GALOFs exhibit nearly diffraction-limited beam quality and a high degree of spatial coherence similar to single-mode fibers [27]. In 2014, image transport through pALOF was first experimentally demonstrated and the transported image quality was proved to be comparable to or better than some of the best commercially available multicore fibers (MCFs) developed for imaging systems [7]. However, the strong signal attenuation in pALOF limits the image transport distance to a few centimeters, too short for most practical applications. Moreover, to further reduce the radius and the sample-to-sample variations of localized beams, the low refractive index contrast is still a bottleneck for pALOF.

To address the shortcomings of pALOF, the next generation of disordered optical fibers should be made from a glass matrix with randomly distributed air holes across the transverse plane [7,28]. As proposed by the earlier work, the filling fraction should be around 50% and the optimal average size of the air holes might be twice the operating wavelength. The large refractive index difference (~0.5) between glass and air can further reduce the radii and sample-to-sample variations of the localized optical modes. In addition, the low optical attenuation in glass materials can extend the imaging transmission distance significantly. The first glass–air-based disordered fiber was reported by Karbasi *et al.* in 2012 [29]. It is fabricated from a porous artisan glass with an average air-filling fraction of ~5%. The size of air holes varies from 0.2 μm to 5.5 μm. Due to the low air-filling fraction and non-uniform distribution of air holes, TAL can only be observed near the boundary of this fiber. To fabricate a glass–air disordered optical fiber with high air-filling fraction and more uniform air-hole distribution, Zhao *et al.* developed a new fabrication recipe based on the stack-and-draw method and demonstrated a low-loss glass–air Anderson localizing optical fiber (GALOF) with an air-filling fraction of ~28% and an average air-hole diameter of ~1.6 μm [12,30]. Using this fiber, they report bending-independent image transport through a meter-long GALOF sample and demonstrate that the quality of images transported through the GALOF is comparable to or even better than that of images transported through commercial MCF for the first time [12].

GALOF-based image transmission can potentially be utilized in fiber-optic endoscopes (FOEs). The most important applications of FOEs are in biomedical research, clinical diagnostics, and surgical operations [31–34]. Most of these applications require the FOEs to provide bending-independent high-fidelity imaging in a minimally invasive way. To satisfy these demanding requirements, GALOF-based FOEs face a number of challenges. First, the structure parameters of GALOFs currently limited by the fabrication process need to be optimized for maximum image quality and resolution. Second, a technique has to be developed that allows for imaging of objects at various distances from the transmission fiber facet. Such a variable working distance should be achieved without requiring distal mechanical scanning heads or other distal bulk optical elements that counteract the minimally invasive character of the fiber-optic probe.

To address these challenges, Zhao *et al.* combine GALOF-based image transmission with image reconstruction based on deep convolutional neural networks (DCNNs). Their FOE features high-fidelity imaging, independence from fiber bending, and lensless imaging up to a depth of a few millimeters [15]. DCNN is a data-driven deep-learning technique, which has gained great success in solving imaging problems recently and demonstrated better performance than the conventional model-based method [15,35–43]. Relying on a large-data based training process, the DCNN can learn the physical process of the image transmission through the entire optical system without knowing any models or priors. It is especially suitable for building GALOF-based FOEs for two main reasons. First, it is extremely difficult to model the imaging process through a meter-long disordered optical fiber, and the numerical simulation of this process requires huge computational power [21]. The DCNN can "learn" the imaging process without any knowledge of the physical system. Second, the DCNN is currently

the optimal choice to truly realize lensless imaging since it can accurately simulate the light propagation through the complete system, from the objects to the final CCD detector. Based on this capability, a DCNN can basically replace any distal optics and other image correction or reconstruction tools.

In the following sections, we review the recent progress in the development of GALOF and GALOF-based imaging systems. In Section 2, the fabrication process, structure parameters, and imaging capabilities of GALOF are shown. In Section 3, recent research on the beam quality of highly localized modes in GALOF is discussed. In Section 4, basic principles and novel experimental results of the GALOF–DCNN-based imaging system are discussed.

2. IMAGE TRANSPORT THROUGH GALOF

The inset in Fig. 1(a_1) shows the SEM image of a typical GALOF cross section. The outer diameter of this GALOF is 414 μm, and the diameter of the disordered structure is 278 μm with an air-filling fraction of 28.5%. GALOFs are fabricated at CREOL using the stack-and-draw method [12,15]. Thousands of silica capillaries are fabricated with different outer and inner diameters. Capillaries are mixed randomly and fed into a jacket to make a preform. Finally, GALOFs with desired sizes are fabricated from canes that are drawn from the preform. With a similar air-filling fraction, the localization length depends on the feature size. Previous numerical investigations using a one-dimensional waveguide model show that feature sizes of about twice the wavelength might give the smallest localization length, which should result in the highest imaging resolution [23]. The air-hole area statistical distributions of three different GALOF samples with similar air-filling fractions are shown in Figs. 1(a_1)–1(c_1). To experimentally measure the localization length, a 635 nm laser beam delivered by a single-mode fiber is butt-coupled into the GALOF samples. The output facet of the GALOF is imaged onto a CCD using a microscope objective. Thirteen different output beam profiles measured for each sample are stacked on top of each other to create one single image per GALOF as shown in Figs. 1(a_2)–1(c_2). For each beam profile, the localization length ξ can be calculated using the following formula [44]:

$$\frac{1}{\xi^2} = \frac{\int I(x,y)^2 \mathrm{d}x\mathrm{d}y}{\left[\int I(x,y)\mathrm{d}x\mathrm{d}y\right]^2}, \tag{1}$$

where ξ is the localization length, and $I(x,y)$ is the beam intensity at position (x, y). A good estimation of the average localization length has been obtained by averaging the 13 calculated values for each GALOF. They are 5.2 μm, 5.4 μm, and 6.8 μm for GALOF(1), GALOF(2), and GALOF(3), respectively. The corresponding feature sizes with maximum statistical distributions are about 1.6 μm, 2.6 μm, and 4.3 μm for GALOF(1)–GALOF(3), respectively. Therefore, it is experimentally confirmed that the localization length decreases with feature size [12]. In addition, the far-field emission angle at the output end has been measured for a number of beam-coupling positions. This angle varies slightly from position to position indicating that there is not one well-defined numerical aperture for GALOFs. However, the observed average far-field emission angle around 11.5 deg provides at least experimental information that can be used for imaging system design and performance evaluation.

The smaller localized beam radius in GALOF(1) makes it a preferable candidate for imaging devices. Using the resolution test target and experimental setup shown in Fig. 2(a), the image transport capability and spatial resolution can be evaluated.

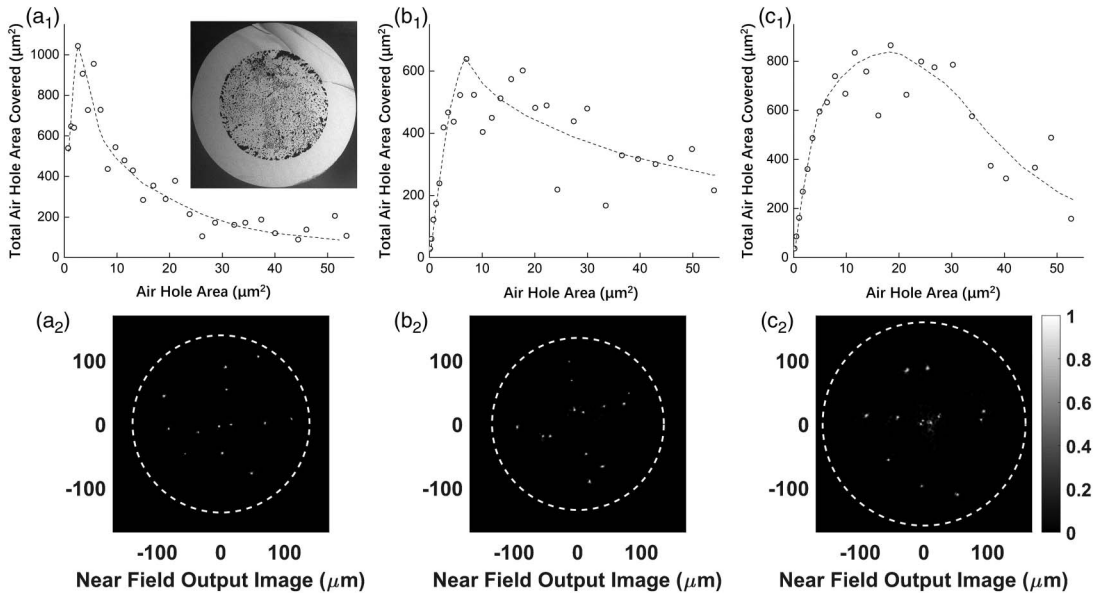

Fig. 1. (a_1)–(c_1) Statistical distributions of air-hole areas in the GALOF samples with similar air-filling fractions. (a_1) GALOF(1), (b_1) GALOF(2), and (c_1) GALOF(3). The SEM image of GALOF(1) is shown in (a_1). (a_2)–(c_2) Near-field output images for multiple excitation positions recorded after transmission through GALOF(1), GALOF(2), and GALOF(3), respectively. The length of all fiber segments is 4.5 cm, and the data are taken at a wavelength of 635 nm [12].

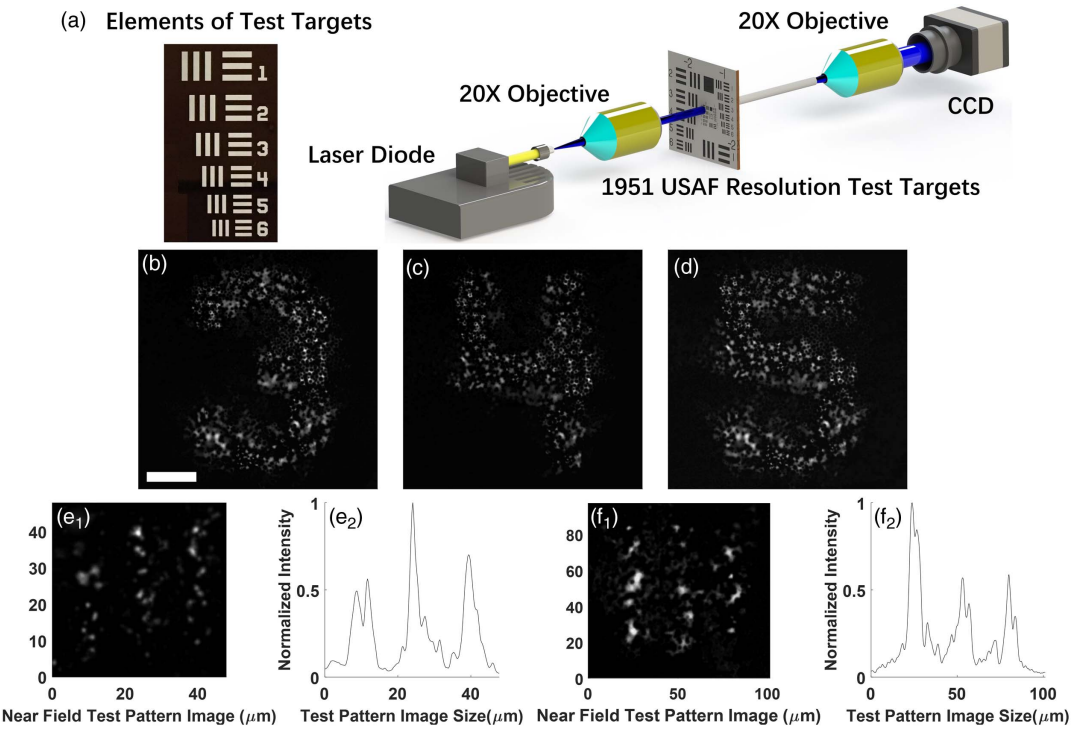

Fig. 2. (a) Experimental setup for image transport. Various elements of resolution test targets are illuminated by a collimated beam from a CW laser diode with a wavelength of 405 nm. The light transmitted through the target elements is coupled into the disordered region of GALOF(1), and the output facet of the fiber is imaged onto a CCD camera. (b)–(d) Transported images of different numbers of group 3 on the 1951 resolution test target using a 4.5-cm-long sample. The length of the scale bar in (b) is 40 μm. (e)–(f) Images of the smallest resolvable line elements of the resolution test targets and the corresponding intensity profiles of the line elements after transport through a GALOF(1) sample. (e_1)–(e_2) are obtained from a 4.5-cm-long sample. The line elements in (e_1) belong to group 6 number 1 on the resolution test target with a line width of 7.8 μm; the integrated cross sections in (e_2) are obtained by integration along the line elements. The visibility value $(I_{max} - I_{min})/(I_{max} + I_{min})$ for the data in (e_2) is about 0.77. (f_1)–(f_2) are obtained from a 90-cm-long sample. The line elements in (f_1) come from group 5 number 2 on the resolution test target. The visibility of (f_2) is about 0.73 [12,15].

Figures 2(b)–2(d) are images of numbers on the resolution test target transported through a 4.5-cm-long GALOF(1) sample. The transmitted images have high visual quality and the same size as the original target elements. To quantify the resolution limit for transportation through the GALOF, line elements on the resolution test targets are transported through samples of different lengths. The smallest line elements that can be resolved are recorded with the CCD camera. As shown in Figs. 2(e) and 2(f), the spatial resolution of a 4.5-cm-long GALOF(1) sample is ∼8 μm, while it is ∼14 μm for a 90-cm-long GALOF(1) segment. The degradation of resolution for a longer piece of sample is attributed to slight variations along the longitudinal direction due to fabrication imperfections. The resolution of GALOF(1) is comparable to some of the best commercial MCF bundles [12]. GALOFs potentially have several advantages over MCFs. First, there exist more modes in GALOFs than in MCFs. The number of localized modes inside GALOF(1) is on the order of 10^6 [27]. The MCF bundle with comparable flexibility and size can only support $\sim 10^4$ modes [45,46]. Although the number of modes in some commercial MCFs can reach 10^5 (Fujikura FIGH-100-1500N), their huge diameters (∼1.5 mm) make the fiber bundle non-flexible and entail a high risk for collateral penetration damage in biological objects. Second, the crosstalk between individual cores of MCFs results in a degradation of the point spread function with increasing transmission distance. In GALOFs, the point spread function is directly related to the localization length, which is independent of the transmission distance [25]. In addition, the cost of GALOFs is potentially lower than the cost of MCFs since GALOFs require only a single material and the fabrication process is straightforward. In contrast, MCFs require expensive highly doped materials to increase the numerical aperture of the individual cores to suppress the crosstalk [47,48]. Moreover, it requires multiple stack-and-draw procedures to fabricate a high-quality MCF bundle [47,48]. This complicated process is reduced to only two steps for fabricating GALOFs: (1) draw silica canes from preforms and (2) draw GALOFs from canes [12]. Over all, the GALOF is the first disordered optical fiber that exhibits all features for practical applications and has the potential for performance superior to conventional MCF imaging bundles.

Besides the characterization of spatial resolution, quantitative evaluations of transported image qualities further confirm that (1) the imaging quality of the GALOF is comparable to some of the best commercial MCFs, (2) GALOF-based imaging is bending-independent, and (3) shorter wavelengths can

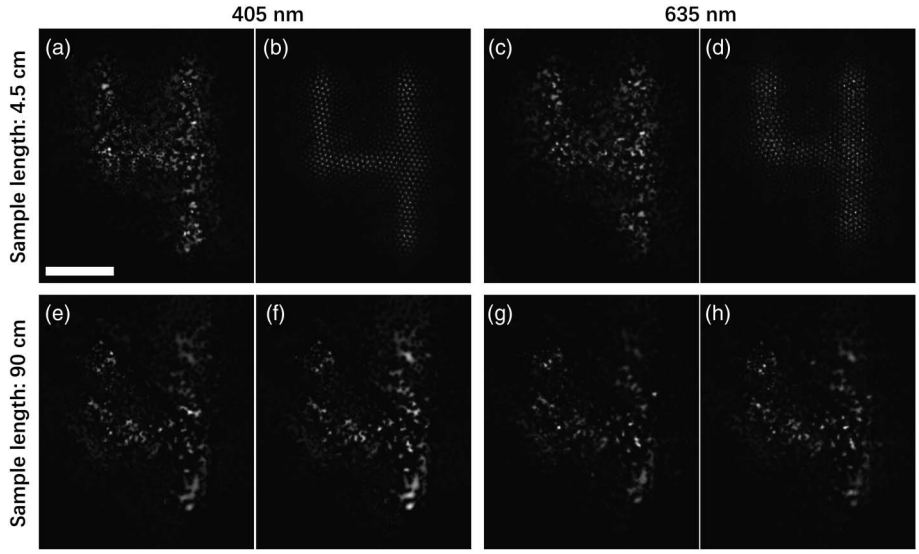

Fig. 3. (a)–(h) Images of digit "4" from group 3 on the 1951 resolution test targets after transport through different fiber samples with different illumination wavelengths. The length of the scale bar in (a) is 50 μm. (a)–(d) are obtained from 4.5-cm-long samples, and (e)–(h) are obtained from 90-cm-long samples. The wavelength for (a), (b), (e), and (f) is 405 nm, while the wavelength for (c), (d), (g), and (h) is 635 nm. (b) and (d) Images transported through commercial imaging fiber FIGH-10-500N. (a), (c), and (e)–(h) Images transported through GALOF(1) samples of different lengths. (e) and (g) are obtained keeping the GALOF(1) straight, while (f) and (h) are obtained using the same sample with a 180 deg turn (20 cm bending radius) [12].

improve imaging quality [12]. Figure 3 lists transported sample images for quantitative evaluations and a comparison between GALOF(1) samples and the commercial imaging fiber sample. Based on the experimental results, two widely used metrics, the mean square error (MSE) and the mean structural similarity index (MSSIM), are introduced to quantify the imaging quality. MSE is defined as follows [49]:

$$\mathrm{MSE} = \frac{1}{M \times N} \sum_{i=1}^{N} \sum_{j=1}^{M} (X_{i,j} - Y_{i,j})^2, \tag{2}$$

where X and Y are two 2D matrices that contain pixel intensities of distorted and reference images, respectively. M and N stand for the sizes of the matrices. MSSIM is calculated by averaging the structural similarity index (SSIM) [49,50]. The SSIM is applied to compare the local image patches between the distorted image X and the reference image Y. It is defined as follows:

$$\mathrm{SSIM}(X, Y) = \frac{(2\mu_X\mu_Y + C_1)(2\sigma_{XY} + C_2)}{(\mu_X^2 + \mu_Y^2 + C_1)(\sigma_X^2 + \sigma_Y^2 + C_2)}. \tag{3}$$

μ_X and μ_Y are the local mean intensities of X and Y. σ_X and σ_Y are the local standard deviations of images X and Y. σ_{XY} is the cross correlation of X and Y. C_1 and C_2 are defined as $(K_1L)^2$ and $(K_2L)^2$, respectively. L is the dynamic range of the image. K_1 and K_2 are two constants, and $K_1, K_2 \ll 1$. These constants are used to avoid unstable results and are somewhat arbitrary. The SSIM index is not sensitive to the variation of their values. Based on the definition of SSIM, MSSIM is calculated by Eq. (4) as follows:

$$\mathrm{MSSIM}(X, Y) = \frac{1}{M} \sum_{j=1}^{M} \mathrm{SSIM}(x_j, y_j). \tag{4}$$

In Eq. (4), x_j and y_j are the image contents at the jth local window of the distorted image X and reference image Y, respectively. The number of local windows is M.

The MSE and MSSIM values of Fig. 3 are listed in Tables 1 and 2, where higher MSE or lower MSSIM values indicate decreased imaging quality. Refer to Table 1; comparing the MSE and MSSIM values under the same wavelength, the GALOF(1) sample demonstrates better imaging performance than the commercial MCF. Refer to the data in both Tables 1 and 2; the imaging quality is lowered when increasing the wavelength for the same fiber sample. For the disordered optical fiber, the origin of this wavelength dependence needs to be further investigated. There is no evidence that the imaging quality is directly linked to the localization length. Therefore, it does not conflict with the recent study that demonstrates that the localization length is wavelength independent [51]. For commercial imaging MCF, it is due to the increased core-to-core coupling. Furthermore, the data listed in Table 2 confirm that strong bending of the GALOF does not noticeably influence the transported image quality. Overall, the quality and resolution of the GALOF compare well with the commercial MCF bundle. Bending-independent imaging makes the GALOF suitable for making a practical optical fiber endoscope where

Table 1. MSE and MSSIM Values of Transported Images for 4.5-cm-Long Fiber Samples[a]

	GALOF(1)		FIGH-10-500N	
λ	405 nm	635 nm	405 nm	635 nm
MSE	0.049	0.055	0.053	0.056
MSSIM	0.317	0.252	0.315	0.237

[a]From [12].

Table 2. MSE and MSSIM Values of Transported Images for 90-cm-Long GALOF(1) Sample[a]

	Straight		Bend	
λ	405 nm	635 nm	405 nm	635 nm
MSE	0.053	0.060	0.051	0.060
MSSIM	0.246	0.206	0.306	0.215

[a]From [12].

flexibility is extremely important. In addition, Zhao *et al.* also experimentally investigate the impact of the GALOF average feature size on the image quality [12]. The digit "4" from group 3 in the resolution target is sent into GALOF(1), GALOF(2), and GALOF(3), respectively. The imaging qualities of all three different samples are calculated using both the MSE and MSSIM methods. The data provided evidence for a general trend of image quality degradation with increasing air-hole sizes. Their observation matches previous numerical simulation results [21,23].

3. HIGH-QUALITY WAVEFRONT IN GALOF

Recently, it has been shown by Abaie *et al.*, both numerically and experimentally, that a large number of localized modes in GALOF exhibit high-quality wavefronts and high spatial coherence, making these transmission channels comparable to single-mode optical fibers [27]. The GALOF sample used in Abaie's work is very similar to GALOF(1) in Fig. 1. They first calculated the localized modes in the GALOF and evaluated their beam quality. For their numerical calculations they used the finite element method and extracted the geometrical GALOF parameters from a SEM image. A working wavelength of 632.8 nm is chosen to match the wavelength of the He–Ne laser used in the experiment. To obtain the M^2 value for the mode quality analysis, modes are numerically propagated in free space after leaving the GALOF using a fast Fourier transform algorithm. The beam waist in the Cartesian coordinates $x(y)$ is calculated by $w_x = 2\sigma_x (w_y = 2\sigma_y)$, where σ_x (σ_y) is the standard deviation of the mode intensity profile. M^2 values (M_x^2, M_y^2) are then obtained using the variance method [27]. An M^2 value of ~1 is strong evidence of nearly diffraction-limited beam quality. The obtained simulation results are shown in Fig. 4.

The results shown in Fig. 4(a) demonstrate that $M^2 < 2$ modes are statistically dominant in the GALOF indicating the presence of abundant localized modes with high-quality wavefronts. The distribution of the corresponding transverse positions within the GALOF cross section is shown in Fig. 4(b). A relatively uniform distribution can be observed, while some local hot spots also exist. The existence of those non-uniform areas might be attributed to the non-uniformity of air-hole sizes and air-filling fractions across the GALOF profile. The regions in GALOF with low air-filling fractions can reduce the number of high-quality modes. This observation is further confirmed by simulation using an optimally designed refractive index profile shown in Fig. 4(c). The size of unit cells in this cross section is 1 μm. Air and glass are mixed randomly with an equal probability to reach a uniform 50% air-filling fraction. The histogram of M^2 values for nearly 500 modes and their position distribution across the fiber cross section are shown in Figs. 4(d) and 4(e). Modes with M^2 values smaller than 2 are much more dominant when compared to the real GALOF calculations shown in Fig. 4(a). Simultaneously, the uniformity of modes distribution is also greatly improved.

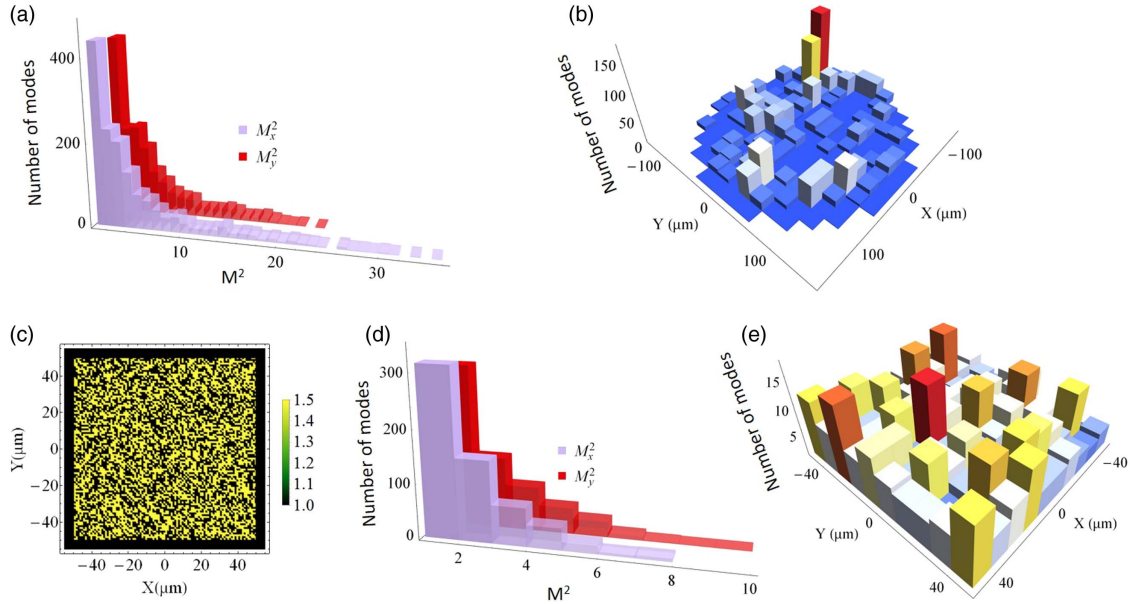

Fig. 4. (a) Histogram of numerically calculated M^2 values for 1500 localized modes in the real GALOF. The vertical axis in (a) represents the total number of modes for different M^2 values. (b) Density histogram of the positions of the modes in (a) within the GALOF cross section. The value of each pixel in (b) corresponds to the number of localized modes. (c) Refractive index profile of an optimally designed GALOF with a 50% air-filling fraction. (d) Histogram of numerically calculated M^2 values for nearly 500 localized modes based on (c). (e) Corresponding density histogram of the mode positions across the profile shown in (c) [27].

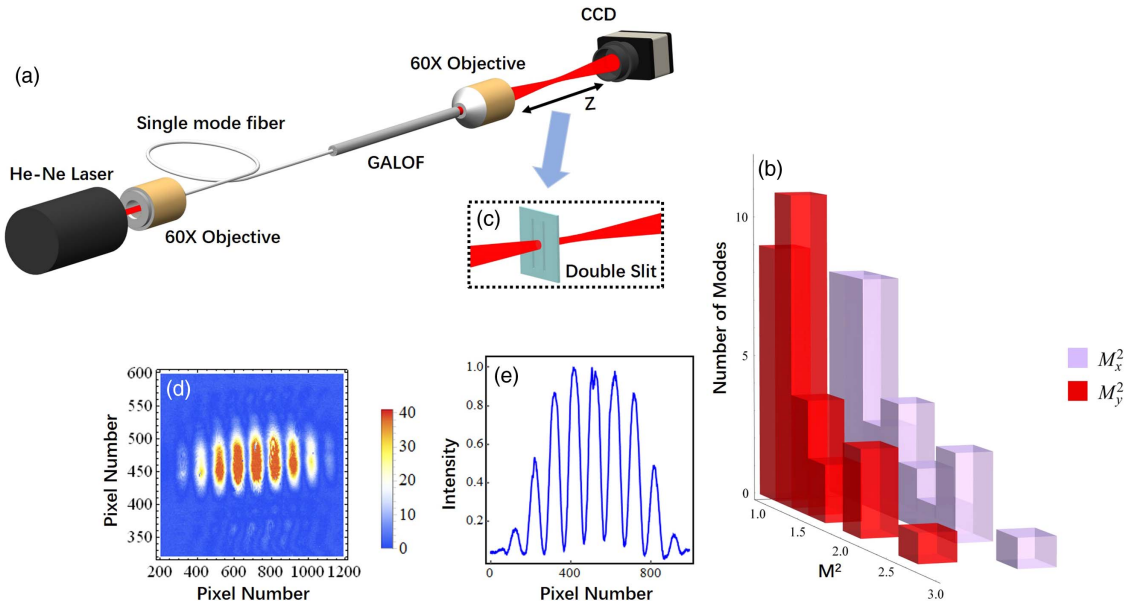

Fig. 5. (a) Experimental setup for M^2 measurements. A He–Ne laser beam is coupled into a single-mode fiber and butt-coupled to the input facet of a 155-cm-long GALOF. The single-mode fiber is scanned across the input facet to excite various localized modes. Beam profiles located at different positions along the z axis are recorded by a CCD beam profiler to extract M^2 values. (b) Histogram of M^2 values for 30 localized modes measured in the experiment. (c) Double slit (slit separation, 500 μm; slit width, 80 μm) inserted in the same setup for spatial coherence evaluation. (d) Interference pattern generated by the localized mode. (e) Intensity distribution averaged over the vertical direction of the pattern in (d) [27].

These calculations indicate that uniform distributions of air-hole size and high air-filling fraction enhance the localization strength and the mode quality. The simulations provide guidance for future GALOF developments and are encouraging regarding potential improvements in GALOF performance.

Experimental investigations also support the numerical simulation results [27]. The experimental setup shown in Fig. 5(a) is applied to excite localized modes and evaluate their M^2 values. The measured M^2 value distributions of 30 modes are shown in Fig. 5(b). Most modes exhibit $M^2 < 2$. Besides a low M^2 value, another unique feature related to high-quality wavefronts is a high degree of spatial coherence. To demonstrate the spatial coherence, one localized mode is excited and used to illuminate the double slit inserted in the output beam path; see Fig. 5(c). The far-field interference pattern generated by the mode after passing through the double slit is shown in Fig. 5(d). Figure 5(e) shows the corresponding vertically averaged intensity distribution. High-contrast interference fringes in Figs. 5(d) and 5(e) indicate the high degree of spatial coherence for the localized mode.

Due to its large transverse size, the GALOF possesses several thousands of modes. The existence of abundant high-quality localized modes gives rise to the high potential of GALOF for imaging applications. These localized modes can be easily excited without the assistance of complicated and expensive spatial light modulators (SLMs) and applied to encode and transport imaging information. The high-quality wavefronts and the large degree spatial coherence of the localized modes result in single-mode-like properties making the GALOF transmission properties remarkably robust with respect to external perturbations. Theoretical analysis indicates that further improvements regarding mode quality are possible in further optimized GALOFs, demonstrating the GALOF potential for next-generation fiber endoscopes.

4. DEEP-LEARNING IMAGING THROUGH GALOF

Imaging systems merely relying on GALOF are faced with a number of challenges, such as artifacts in the transported images and a fixed working distance. The DCNN is able to address all these issues by "learning" the imaging transfer process [15]. To generate a computational architecture that can map the transported raw images to their corresponding input images requires a training process for the DCNN. The training process requires a large number of image pairs. Each image pair consists of a matched input image (ground truth) and a corresponding raw image transported through the imaging system. In the training phase, the DCNN is initialized randomly using a Gaussian distribution. Then a batch of raw images is sent into the DCNN to generate corresponding output images. The DCNN is trained by optimizing the parameters through minimizing the loss function based on the difference between the output images generated in the training process and the original input images. The loss function is defined using the mean absolute error (MAE) metric. The MAE is expressed as $|I_{\text{rec}} - I_{\text{ref}}|/(wh)$. I_{rec} and I_{ref} are the reconstructed image intensity and the input image intensity, respectively. w and h are the width and the height of the images. When the loss of the DCNN finally converges, the training process is finished and the parameters of the DCNN are fixed. In the test phase, the trained DCNN is applied to reconstruct images from the raw data that never appear in the training data. To evaluate the performance of the trained DCNN, reconstructed test images are

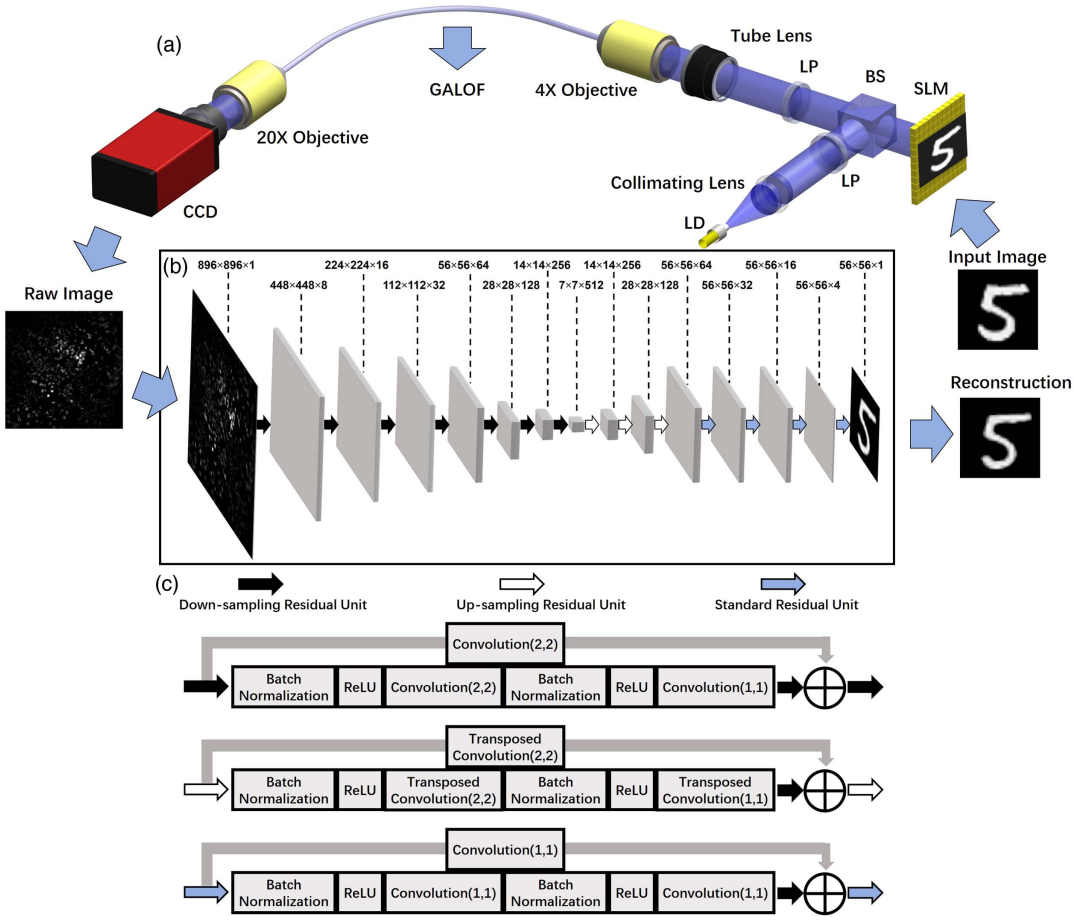

Fig. 6. (a) Schematic of deep-learning-based imaging experimental setup (LD, 405 nm laser diode; LP, linear polarizer; BS, beam splitter; SLM, spatial light modulator). The pixel size of the SLM is 9.2 μm × 9.2 μm, and the total number of pixels of the SLM is 1920 × 1152. The pixel size of the CCD is 6.45 μm × 6.45 μm, and the total number of pixels of the CCD is 1388×1038. The fiber used here is a 90-cm-long GALOF(1) sample. In (a) the SLM is illuminated by a collimated laser beam delivered by a single-mode fiber. The SLM is modulated by 8-bit gray-scale input images obtained from the Modified National Institute of Standards and Technology (MNIST) database of handwritten digits. Being located between two linear polarizers with the same polarization, the SLM creates intensity objects that are resized to a matrix of 56 × 56 pixels. Then the intensity objects are de-magnified and imaged onto the GALOF(1) input facet by a combination of a tube lens and a 4× objective. The CCD records the raw image of the output facet of the GALOF(1) sample. The raw images are cropped to a size of 896 × 896 for processing. (b) Architecture of the DCNN. The DCNN is trained by 4000 image pairs (input images and corresponding transported raw images). After the training process, the DCNN can recover test objects from raw test images recorded by the CCD in the test phase. Five-hundred different image pairs serve as test data. (c) shows the detailed structures of residual units corresponding to the arrows in the top row of (c) [15].

compared with the corresponding input test images by the MAE method. Figure 6(a) demonstrates the experimental procedure to generate the training and test data. Based on the work reported by Zhao *et al.* [15], a set of 4000 different images from the MNIST database is sent into the SLM, and the transported raw intensity images are recorded by a CCD. These 4000 image pairs serve as the training data. Another separate set of 500 image pairs is used as test data. The architecture of the DCNN is illustrated in Fig. 6(b). The DCNN first extracts high-dimensional features from the loaded raw intensity image through seven down-sampling residual units. Subsequently, another three up-sampling residual units followed by four standard residual units reconstruct the output image, which is an estimation of the original input intensity image. The details of each residual unit are given in Fig. 6(c). The size of all the filters used in the convolutional operations is 3 × 3. The training time is about 38 min based on two GPUs (GeForce GTX 1080 Ti). The reconstruction time is about 4 ms per test image. The short reconstruction time demonstrates that the DCNN-based GALOF imaging system has the potential to perform video-rate real-time imaging.

Figure 7 shows sample test results and error analysis based on the DCNN/GALOF scheme proposed by Zhao *et al.* [15]. The input images located at different working distances shown in Figs. 7(a_1)–7(c_1) are collected with just a cleaved fiber input end. The experiments are repeated for both straight GALOF and bent GALOF while the DCNN model is the same one and is trained just using the data collected from the straight GALOF. Comparing the input images with the reconstructed images, it is apparent that the DCNN/GALOF system can recover the true images remarkably well. A further quantitative error analysis for the test process is shown in Fig. 7(d). The low

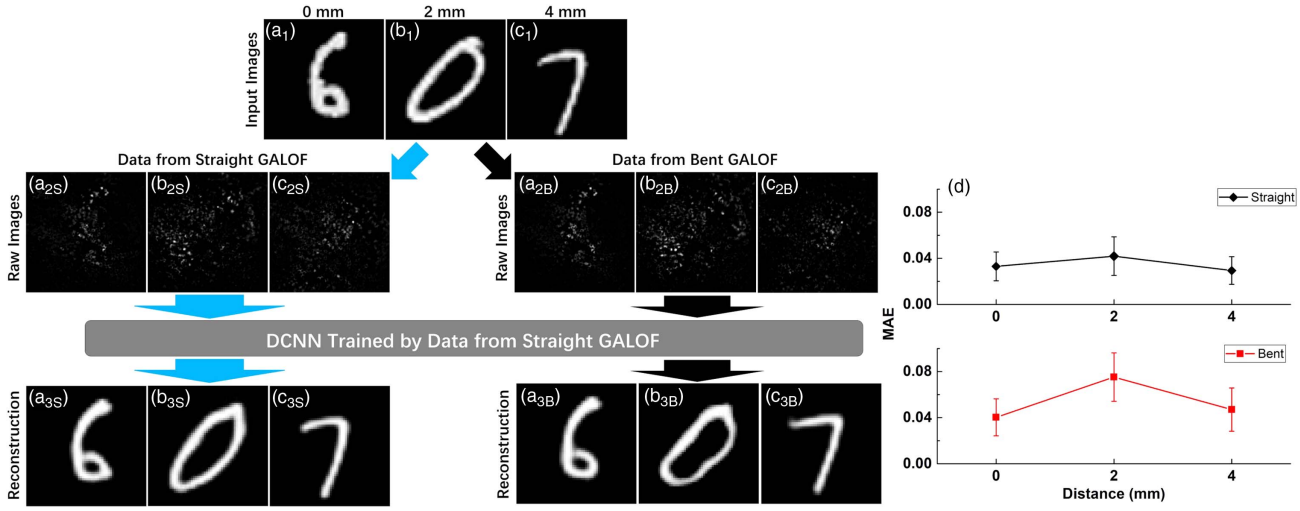

Fig. 7. (a_1)–(c_1) Three test input images located at different working distances, ranging from 0 mm to 4 mm. The blue arrow and the black arrow indicate the reconstruction processes for data collected from the straight and the bent states of the same 90-cm-long GALOF(1) sample, respectively. For the bent state, the bending angle is 90 deg. The DCNN used here is trained just once by the training data collected from the straight fiber. (a_{2S})–(c_{2S}) Raw intensity images collected from the straight fiber. (a_{2B})–(c_{2B}) Raw intensity images collected from the bent fiber. (a_{3S})–(c_{3S}) Reconstructed images from raw intensity images (a_{2S})–(c_{2S}). (a_{3B})–(c_{3B}) Reconstructed images from raw intensity images (a_{2B})–(c_{2B}). (a_{2S})–(a_{3S}) and (a_{2B})–(a_{3B}) are obtained when the working distance is 0 mm. (b_{2S})–(b_{3S}) and (b_{2B})–(b_{3B}) are obtained for 2 mm working distance. (c_{2S})–(c_{3S}) and (c_{2B})–(c_{3B}) are obtained for 4 mm working distance. (d) Averaged MAE and the corresponding standard deviation of the 500 test images for both straight GALOF and bent GALOF [15].

MAE error proves that the trained DCNN models the underlying physics of the imaging system accurately. Based on the results in Fig. 7, the main advantages of DCNN/GALOF system can be summarized as follows. First, the system can deliver artifact-free images without any distal optics for various working distances. This capability allows us to reduce the imaging unit to the diameter of the fiber itself so that any penetration damage can be minimized when performing *in vivo* imaging. Furthermore, being able to deliver the image of the object at considerable working distance would further avoid the contact damage especially for *in vivo* studies of neural activity. Second, the imaging process of the DCNN/GALOF system is bending-independent so that the DCNN model trained using data from a certain fiber state can be applied to perform high-fidelity reconstruction of images transported by any other fiber state. This is in striking contrast to multimode fiber (MMF) imaging systems. Current MMF-based imaging systems mainly rely on the transmission matrix method to perform image reconstructions [34,52–54]. However, the transmission matrix is extremely sensitive to external perturbations. Tiny shifts or bending (a few hundred micrometers) of the MMF can impair the imaging process unless a recalibration of the transmission matrix is performed, or very precise knowledge of the bending state and its shape is known [54]. Recently, DCNNs have also been reportedly used for image reconstruction and classification after propagation through MMF [40,41,43]. Similar to the concept applied in DCNN/GALOF systems, DCNNs are explored to learn the image transfer processes through MMFs so that images of objects can be recovered from measured speckle patterns. Unfortunately, current DCNN-based MMF systems are very vulnerable to environmental changes such as fiber bending or temperature variations since the multimode inference effects inside the MMFs are inherently extremely sensitive to any refractive index changes limiting the robustness of such systems.

The abovementioned DCNN is also able to transfer its learning capability to reconstruct objects that belong to classes different from the training objects. As shown in Fig. 8, the DCNN trained by handwritten digits from the MNIST database can be applied to reconstruct English letters. The English letters are from a different domain compared to the handwritten numbers. Although the demonstrated results are mainly based on handwritten numbers and English letters, imaging targets of DCNN/GALOF systems are not limited to binary and sparse objects. Overall, the DCNN/GALOF system is a robust, high-fidelity, and highly functionalized imaging system providing potential benefits for applications in both basic research and clinical diagnosis.

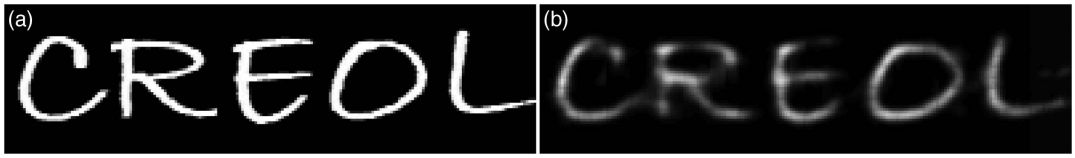

Fig. 8. Transfer-learning reconstruction of English letters. (a) Input image. The working distance is 0 mm, and the GALOF is kept straight. "CREOL" is short for "College of Optics and Photonics." The size of the input image is 56 × 200 pixels. (b) Reconstructed image.

5. CONCLUSIONS

Disordered optical fiber shows great potential for next-generation imaging systems in general and FOEs in particular. We demonstrate high and sometimes superior imaging quality and system capabilities that originate from the special guiding properties in disordered structures due to TAL. Important structural parameters, such as the air-filling fractions and feature sizes, influence the localization strength, which is directly related to the point spread function and resolution of the imaging system. GALOF with large refractive index fluctuations and near-optimal feature sizes demonstrates extraordinary image transport performance. High-fidelity and bending-independent imaging is realized through the GALOF. The current GALOF performance is still limited by the speckle-pattern artifact in the transported image and operation at a fixed working distance. These challenges can be addressed by introducing deep-learning techniques and applying them to an imaging reconstruction process. Future efforts will focus on exploring improved GALOF designs and fabrication, as well as the development of more efficient deep-learning algorithms in particular for the reconstruction of complex biological objects.

REFERENCES

1. P. W. Anderson, "Absence of diffusion in certain random lattices," Phys. Rev. **109**, 1492–1505 (1958).
2. S. John, "Localization of light," Phys. Today **44**(5), 32–40 (1991).
3. I. S. Graham, L. Piché, and M. Grant, "Experimental evidence for localization of acoustic waves in three dimensions," Phys. Rev. Lett. **64**, 3135–3138 (1990).
4. H. Hu, A. Strybulevych, J. H. Page, S. E. Skipetrov, and B. A. van Tiggelen, "Localization of ultrasound in a three-dimensional elastic network," Nat. Phys. **4**, 945–948 (2008).
5. A. A. Chabanov, M. Stoytchev, and A. Z. Genack, "Statistical signatures of photon localization," Nature **404**, 850–853 (2000).
6. H. Cao, Y. G. Zhao, S. T. Ho, E. W. Seelig, Q. H. Wang, and R. P. H. Chang, "Random laser action in semiconductor powder," Phys. Rev. Lett. **82**, 2278–2281 (1999).
7. S. Karbasi, R. J. Frazier, K. W. Koch, T. Hawkins, J. Ballato, and A. Mafi, "Image transport through a disordered optical fibre mediated by transverse Anderson localization," Nat. Commun. **5**, 3362 (2014).
8. B. Abaie, E. Mobini, S. Karbasi, T. Hawkins, J. Ballato, and A. Mafi, "Random lasing in an Anderson localizing optical fiber," Light: Sci. Appl. **6**, e17041 (2017).
9. T. Crane, O. J. Trojak, J. P. Vasco, S. Hughes, and L. Sapienza, "Anderson localization of visible light on a nanophotonic chip," ACS Photon. **4**, 2274–2280 (2017).
10. O. J. Trojak, T. Crane, and L. Sapienza, "Optical sensing with Anderson-localised light," Appl. Phys. Lett. **111**, 141103 (2017).
11. S. H. Choi, S.-W. Kim, Z. Ku, M. A. Visbal-Onufrak, S.-R. Kim, K.-H. Choi, H. Ko, W. Choi, A. M. Urbas, T.-W. Goo, and Y. L. Kim, "Anderson light localization in biological nanostructures of native silk," Nat. Commun. **9**, 452 (2018).
12. J. Zhao, J. E. A. Lopez, Z. Zhu, D. Zheng, S. Pang, R. A. Correa, and A. Schülzgen, "Image transport through meter-long randomly disordered silica-air optical fiber," Sci. Rep. **8**, 3065 (2018).
13. T. H. Tuan, S. Kuroyanagi, K. Nagasaka, T. Suzuki, and Y. Ohishi, "Near-infrared optical image transport through an all-solid tellurite optical glass rod with transversely-disordered refractive index profile," Opt. Express **26**, 16054–16062 (2018).
14. N. N. Shi, C.-C. Tsai, M. J. Carter, J. Mandal, A. C. Overvig, M. Y. Sfeir, M. Lu, C. L. Craig, G. D. Bernard, Y. Yang, and N. Yu, "Nanostructured fibers as a versatile photonic platform: radiative cooling and waveguiding through transverse Anderson localization," Light: Sci. Appl. **7**, 37 (2018).
15. J. Zhao, Y. Sun, Z. Zhu, J. E. Antonio-Lopez, R. A. Correa, S. Pang, and A. Schülzgen, "Deep learning imaging through fully-flexible glass-air disordered fiber," ACS Photon. **5**, 3930–3935 (2018).
16. A. F. Ioffe and A. R. Regel, "Non-crystalline, amorphous and liquid electronic semiconductors," Prog. Semicond. **4**, 237–291 (1960).
17. H. De Raedt, A. Lagendijk, and P. de Vries, "Transverse localization of light," Phys. Rev. Lett. **62**, 47–50 (1989).
18. T. Schwartz, G. Bartal, S. Fishman, and M. Segev, "Transport and Anderson localization in disordered two-dimensional photonic lattices," Nature **446**, 52–55 (2007).
19. S. Karbasi, C. R. Mirr, P. G. Yarandi, R. J. Frazier, K. W. Koch, and A. Mafi, "Observation of transverse Anderson localization in an optical fiber," Opt. Lett. **37**, 2304–2306 (2012).
20. S. S. Abdullaev and F. K. Abdullaev, "On propagation of light in fiber bundles with random parameters," Radiofizika **23**, 766–767 (1980).
21. S. Karbasi, C. R. Mirr, R. J. Frazier, P. G. Yarandi, K. W. Koch, and A. Mafi, "Detailed investigation of the impact of the fiber design parameters on the transverse Anderson localization of light in disordered optical fibers," Opt. Express **20**, 18692–18706 (2012).
22. S. Karbasi, K. W. Koch, and A. Mafi, "Multiple-beam propagation in an Anderson localized optical fiber," Opt. Express **21**, 305–313 (2013).
23. S. Karbasi, K. W. Koch, and A. Mafi, "Modal perspective on the transverse Anderson localization of light in disordered optical lattices," J. Opt. Soc. Am. B **30**, 1452–1461 (2013).
24. B. Abaie and A. Mafi, "Scaling analysis of transverse Anderson localization in a disordered optical waveguide," Phys. Rev. B **94**, 064201 (2016).
25. S. Karbasi, K. W. Koch, and A. Mafi, "Image transport quality can be improved in disordered waveguides," Opt. Commun. **311**, 72–76 (2013).
26. G. Ruocco, B. Abaie, W. Schirmacher, A. Mafi, and M. Leonetti, "Disorder-induced single-mode transmission," Nat. Commun. **8**, 14571 (2017).
27. B. Abaie, M. Peysokhan, J. Zhao, J. E. Antonio-Lopez, R. Amezcua-Correa, A. Schülzgen, and A. Mafi, "Disorder-induced high-quality wavefront in an Anderson localizing optical fiber," Optica **5**, 984–987 (2018).
28. A. Mafi, "Transverse Anderson localization of light: a tutorial," Adv. Opt. Photon. **7**, 459–515 (2015).
29. S. Karbasi, T. Hawkins, J. Ballato, K. W. Koch, and A. Mafi, "Transverse Anderson localization in a disordered glass optical fiber," Opt. Mater. Express **2**, 1496–1503 (2012).
30. J. Zhao, J. E. Antonio-Lopez, R. A. Correa, A. Mafi, M. Windeck, and A. Schülzgen, "Image transport through silica-air random core optical fiber," in *Conference on Lasers and Electro-Optics*, OSA Technical Digest (online) (Optical Society of America, 2017), paper JTu5A.91.
31. B. A. Flusberg, E. D. Cocker, W. Piyawattanametha, J. C. Jung, E. L. Cheung, and M. J. Schnitzer, "Fiber-optic fluorescence imaging," Nat. Methods **2**, 941–950 (2005).
32. J. T. C. Liu, N. O. Loewke, M. J. Mandella, R. M. Levenson, J. M. Crawford, and C. H. Contag, "Point-of-care pathology with miniature microscopes," Anal. Cell. Pathol. **34**, 81–98 (2011).
33. V. Szabo, C. Ventalon, V. De Sars, J. Bradley, and V. Emiliani, "Spatially selective holographic photoactivation and functional fluorescence imaging in freely behaving mice with a fiberscope," Neuron **84**, 1157–1169 (2014).
34. S. Ohayon, A. Caravaca-Aguirre, R. Piestun, and J. J. DiCarlo, "Minimally invasive multimode optical fiber microendoscope for deep brain fluorescence imaging," Biomed. Opt. Express **9**, 1492–1509 (2018).
35. C. Dong, C. C. Loy, K. He, and X. Tang, "Image super-resolution using deep convolutional networks," IEEE Trans. Pattern Anal. Mach. Intell. **38**, 295–307 (2016).
36. A. Sinha, J. Lee, S. Li, and G. Barbastathis, "Lensless computational imaging through deep learning," Optica **4**, 1117–1125 (2017).
37. Y. Rivenson, Z. Göröcs, H. Günaydin, Y. Zhang, H. Wang, and A. Ozcan, "Deep learning microscopy," Optica **4**, 1437–1443 (2017).
38. S. Li, M. Deng, J. Lee, A. Sinha, and G. Barbastathis, "Imaging through glass diffusers using densely connected convolutional networks," Optica **5**, 803–813 (2018).

39. T. Nguyen, Y. Xue, Y. Li, L. Tian, and G. Nehmetallah, "Deep learning approach for Fourier ptychography microscopy," Opt. Express **26**, 26470–26484 (2018).
40. N. Borhani, E. Kakkava, C. Moser, and D. Psaltis, "Learning to see through multimode fibers," Optica **5**, 960–966 (2018).
41. B. Rahmani, D. Loterie, G. Konstantinou, D. Psaltis, and C. Moser, "Multimode optical fiber transmission with a deep learning network," Light: Sci. Appl. **7**, 69 (2018).
42. M. Lyu, H. Wang, G. Li, and G. Situ, "Exploit imaging through opaque wall via deep learning," arXiv:1708.07881 (2017).
43. P. Fan, T. Zhao, and L. Su, "Deep learning the high variability and randomness inside multimode fibres," arXiv:1807.09351 (2018).
44. M. Leonetti, S. Karbasi, A. Mafi, and C. Conti, "Experimental observation of disorder induced self-focusing in optical fibers," Appl. Phys. Lett. **105**, 171102 (2014).
45. K. L. Reichenbach and C. Xu, "Numerical analysis of light propagation in image fibers or coherent fiber bundles," Opt. Express **15**, 2151–2165 (2007).
46. X. Chen, K. L. Reichenbach, and C. Xu, "Experimental and theoretical analysis of core-to-core coupling on fiber bundle imaging," Opt. Express **16**, 21598–21607 (2008).
47. J. M. Stone, H. A. C. Wood, K. Harrington, and T. A. Birks, "Low index contrast imaging fibers," Opt. Lett. **42**, 1484–1487 (2017).
48. H. A. C. Wood, K. Harrington, T. A. Birks, J. C. Knight, and J. M. Stone, "High-resolution air-clad imaging fibers," Opt. Lett. **43**, 5311–5314 (2018).
49. Z. Wang and A. C. Bovik, "Mean squared error: love it or leave it? a new look at signal fidelity measures," IEEE Signal Process. Mag. **26**, 98–117 (2009).
50. W. Zhou, A. C. Bovik, H. R. Sheikh, and E. P. Simoncelli, "Image quality assessment: from error visibility to structural similarity," IEEE Trans. Image Process. **13**, 600–612 (2004).
51. W. Schirmacher, B. Abaie, A. Mafi, G. Ruocco, and M. Leonetti, "What is the right theory for Anderson localization of light? an experimental test," Phys. Rev. Lett. **120**, 067401 (2018).
52. T. Cizmar and K. Dholakia, "Exploiting multimode waveguides for pure fibre-based imaging," Nat. Commun. **3**, 1027 (2012).
53. Y. Choi, C. Yoon, M. Kim, T. D. Yang, C. Fang-Yen, R. R. Dasari, K. J. Lee, and W. Choi, "Scanner-free and wide-field endoscopic imaging by using a single multimode optical fiber," Phys. Rev. Lett. **109**, 203901 (2012).
54. M. Plöschner, T. Tyc, and T. Čižmár, "Seeing through chaos in multimode fibres," Nat. Photonics **9**, 529–535 (2015).